Article

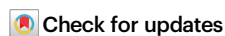# Spectral properties of two superconducting artificial atoms coupled to a resonator in the ultrastrong coupling regime

A. Tomonaga [1,2,6] ✉, R. Stassi[2,3], H. Mukai [1,2], F. Nori [2,4], F. Yoshihara[1,5] & J. S. Tsai[1,2] ✉

We experimentally investigate a superconducting circuit composed of two flux qubits ultrastrongly coupled to a common *LC* resonator. Owing to the large anharmonicity of the flux qubits, the system can be described well by a generalized Dicke Hamiltonian containing spin–spin interaction terms. In the experimentally measured spectrum, we observed two key phenomena. First, an avoided level crossing provides evidence of the exotic interaction that allows the simultaneous excitation of two artificial atoms by absorbing one photon from the resonator. Second, we identified a pronounced spectral asymmetry that is a clear signature of light-matter decoupling. This multi-atom ultrastrongly coupled system opens the door to studying novel processes for quantum optics and quantum-information tasks on a chip.

Superconducting circuits provide a versatile and flexible platform for modeling various quantum systems[1–6]. In this platform, artificial atoms can be designed to have tailored energy transitions and controllable interactions with microwave photons[2]. Moreover, superconducting circuits have also become one of the main platforms for scalable quantum information processing and quantum simulation[2–6].

Taking advantage of the high electromagnetic field in a one-dimensional resonator and the huge dipole moment of artificial atoms, these systems achieve a stronger light–matter interaction than those at bare atomic or resonator frequencies[7–13]. This ultrastrong (deep-strong) interaction might lead to promising applications, such as high-speed and high-efficiency quantum information processing devices[14–19]. In this coupling regime, several unique physical phenomena have been predicted, and now, some of these are realized experimentally.

Important theoretical predictions include, for example, quantum vacuum radiation and entanglement from the ground state[20–24]; multi-excitation exchanges between qubits and resonators[25]; or physical processes analogous to parametric down-conversion[26,27]. In 2016, a theoretical work showed that one photon can simultaneously excite two atoms[28,29]. This effect should be observable if the atoms are ultrastrongly coupled with a cavity mode and the parity symmetry of the atoms is broken. Similar to Rabi oscillations, this is a coherent and unitary process where the atoms can jointly absorb or emit one photon[27,28].

The first realization of the ultrastrong coupling regime in circuit QED[7] was evidenced by an avoided level crossing, indicating the exchange of excitations between the qubit and two cavity modes; namely, the multi-excitation exchange between one flux qubit and a waveguide resonator. Later, it was shown[30,31] that, when the parity symmetry is broken in an atom-light system in the ultrastrong coupling regime, the light field acquires a coherence in the ground state that induces symmetry breaking in an ancillary flux qubit weakly coupled to the same field.

Here, we experimentally investigate a circuit composed of two flux qubits ultrastrongly coupled to a common *LC* resonator. Flux qubits, which form artificial atoms, share the same inductor with the *LC* resonator, consequently they interact with each other. This system is described by the Dicke Hamiltonian, generalized to include atomic longitudinal couplings and spin–spin interaction terms.

[1]Department of Physics, Tokyo University of Science, Shinjuku, Tokyo, Japan. [2]Center for Quantum Computing, RIKEN, Wakoshi, Saitama, Japan. [3]Dipartimento di Scienze Matematiche e Informatiche, Scienze Fisiche e Scienze della Terra, Università di Messina, Messina, Italy. [4]Physics Department, The University of Michigan, Ann Arbor, Michigan, USA. [5]Advanced ICT Research Institute, National Institute of Information and Communications Technology, Koganei, Tokyo, Japan. [6]Present address: National Institute of Advanced Industrial Science and Technology (AIST), Tsukuba, Ibaraki, Japan. ✉e-mail: akiyoshi.tomonaga@aist.go.jp; tsai@riken.jp

In the measured spectrum, away from the flux qubit optimal point (where the parity symmetry of the system is broken), we observe an energy-level anticrossing, which indicates hybridization between the states $|gg1\rangle$ and $|ee0\rangle$, where $|g\rangle$($|e\rangle$) and $|0\rangle$ respectively indicate the atomic ground (excited) and zero photon states. This is the fingerprint of the interaction that allows one photon to simultaneously excite two atoms, as well as the reverse process. Here, when the system is set up in the one-photon state, the artificial atoms and the resonator can exchange excitations exhibiting Rabi-like oscillations.

Since the atom–light and atom–atom interactions are very strong, the system states should be strongly hybridized, and the clear observation of the "one–photon–exciting–two–atoms" effect would not be straightforward. However, by studying the generalized Dicke Hamiltonian, we found (i) a partial suppression of the transverse interaction given by a competition between the spin–spin interaction and the spins–light interaction and (ii) the "decoupling" of the longitudinal interaction that depends on the sign of the external flux bias. The decoupling justifies the asymmetry in the measured spectrum.

While a multimode cavity coupled to a single atom, as in[7], allows frequency-selective interactions, its photon conversion capability is limited by mode spacing. In contrast, multiple atoms coupled to a single cavity (as in our work) can facilitate the conversion of a single photon into multiple lower-frequency excitations. Despite superficial similarities, these two circuits are different in configuration and serve distinct roles.

On the other hand, a recent experiment[32] based on many-body localization (MBL), not studied in our work, shows the suppression of the photon down-conversion, due to MBL. This is in stark contrast to our system, which is designed to actively promote both down- and up-conversion processes. Moreover, ref. [32] operates in what they call superstrong coupling regime, which arises when the atomic linewidth exceeds the cavity mode spacing. The resulting three-wave mixing interaction induces multiphoton processes across many modes, which is not our case.

Furthermore, ultrastrong coupling, as realized in our work, occurs in a different regime: when the light-matter coupling strength exceeds 10% of the cavity photon energy. This system is described by a generalized Dicke Hamiltonian including counter-rotating terms, leading to strong hybridization of the qubits with a cavity mode.

Results
Device
Figure 1a shows an optical microscopy image of the artificial-atom–resonator circuit. The *LC* resonator is composed of an inter-digital capacitor and a line inductor made of a superconducting thin film[33,34]. The two flux qubits are inductively coupled to the *LC* resonator via a Josephson junction (Fig. 1b), which increases the strength of couplings to the ultrastrong regime. Small dots around the two qubits are flux traps that prevent vortex fluctuations during the measurements[35]. The energies of the flux qubits[36] can be changed by applying an external magnetic flux to the loop from a global coil and using an on-chip bias line. Figure 1c shows the equivalent circuit with lumped elements and Josephson junctions.

The Hamiltonian of the entire system is[37–39]

$$\hat{\mathcal{H}}_{tot} = \hat{\mathcal{H}}_{q1} + \hat{\mathcal{H}}_{q2} + \hat{\mathcal{H}}_r + \hat{\mathcal{H}}_{int}, \tag{1}$$

where $\hat{\mathcal{H}}_{qk}$ ($k = 1, 2$), $\hat{\mathcal{H}}_r$, and $\hat{\mathcal{H}}_{int}$ represent the qubits, resonator, and atom–atom couplings, respectively. The Hamiltonian of the resonator is $\hat{\mathcal{H}}_r = \hbar\omega_r(\hat{a}^\dagger\hat{a} + 1/2)$, where $\omega_r \equiv 1/\sqrt{L_r C_r}$ is the resonance frequency, $\hat{a} \equiv (\hat{\phi}_r - iZ_r\hat{q}_r)/\sqrt{2\hbar Z_r}$ is the annihilation operator, $Z_r = \sqrt{L_r/C_r}$ is the characteristic impedance of the *LC*
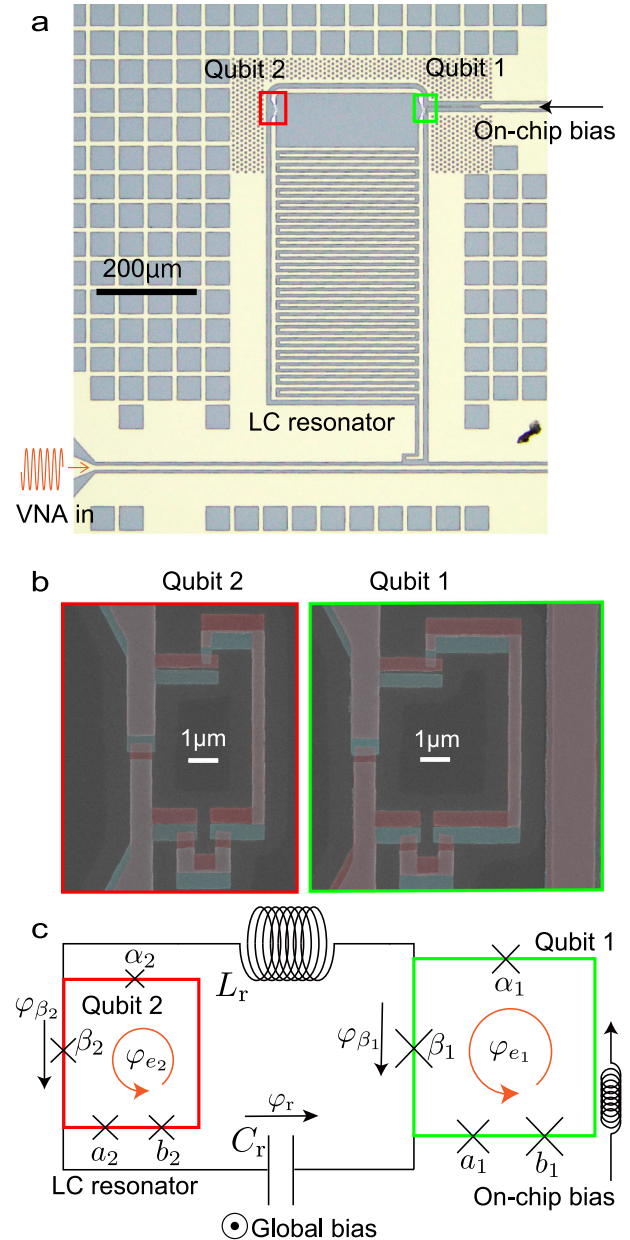

Fig. 1 | Device. a Optical microscopy image of the measured sample. The sample holder has a coil to bias a uniform magnetic field from the back surface of the chip. Qubit 1 has a local bias line that changes the magnetic flux of the qubit loop. The spectrum is measured using a vector network analyzer (VNA) for probing and reading from the transmission line shown below the circuit. **b** False-color SEM images of qubits 1 and 2. The design parameters of both qubit junctions are the same. Different colors represent different layers of aluminum deposited via double-angle shadow evaporation. **c** Equivalent circuit diagram of the sample. The symbols α_i, β_i, a_i, and b_i ($i \in \{1, 2\}$) label each Josephson junction, while φ denotes the phase difference across a circuit component.

resonator, and $\hat{q}_r$ is the conjugate variable of $\hat{\phi}_r = \Phi_0\hat{\varphi}_r$. Here, Φ_0 is the flux quantum and the flux φ_r is defined in Fig. 1c. The Hamiltonian of the k-th artificial atom is

$$\hat{\mathcal{H}}_{qk} \equiv 4E_{ck}\hat{\mathbf{q}}_k^T\mathbf{M}_k^{-1}\hat{\mathbf{q}}_k + E_{Lr}\hat{\varphi}_{\beta k}^2 + \hat{\mathcal{U}}_{Jk}, \tag{2}$$

where E_{ck} is the charging energy of the Josephson junction a_k (see Fig. 1b and 1c), $\varphi_{\beta k}$ represents the phase differences in each β-junction of qubits, $\mathbf{M}_k$ is the normalized mass matrix, $E_{Lr} = \Phi_0^2/(2L_r)$, and $\hat{\mathcal{U}}_{Jk}$ is

the qubit potential energy of Josephson junctions:

$$\hat{\mathcal{U}}_{Jk}(\hat{\varphi}_{ek}) = -E_{Jk}\left[\beta_k\cos(\hat{\varphi}_{\beta k}) + \cos(\hat{\varphi}_{ak}) + \cos(\hat{\varphi}_{bk}) + \alpha_k\cos(\varphi_{ek} - \hat{\varphi}_{ak} - \hat{\varphi}_{bk} - \hat{\varphi}_{\beta k})\right]. \quad (3)$$

Here, E_{Jk} is the current energy of the Josephson junction a_k, φ_{ik} ($i = \alpha, a, b$) are the phase differences in each junction α_k, a_k, and b_k, and φ_{ek} represents the external flux for the loop of each atom. The interaction Hamiltonian

$$\hat{\mathcal{H}}_{int} = -E_{Lr}(\hat{\varphi}_{\beta 1}\hat{\varphi}_r - \hat{\varphi}_{\beta 2}\hat{\varphi}_r + \hat{\varphi}_{\beta 1}\hat{\varphi}_{\beta 2}) \quad (4)$$

is obtained from the boundary condition (Kirchhoff's voltage law) of the loop forming the resonator with the elements L_r and C_r.

By approximating each atom as a two-level system[40] on the basis of persistent currents of the superconducting loop, we obtain the total Hamiltonian in Eq. (1) as

$$\hat{\mathcal{H}}_{tot}/\hbar \simeq \omega_r\hat{a}^\dagger\hat{a} + \frac{\varepsilon_1}{2}\hat{\sigma}_{z1} + \frac{\Delta_1}{2}\hat{\sigma}_{x1} + \frac{\varepsilon_2}{2}\hat{\sigma}_{z2} + \frac{\Delta_2}{2}\hat{\sigma}_{x2} - (g_1\hat{\sigma}_{z1} - g_2\hat{\sigma}_{z2})(\hat{a}^\dagger + \hat{a}) - \frac{2g_1g_2}{\omega_r}\hat{\sigma}_{z1}\hat{\sigma}_{z2}, \quad (5)$$

where ε_k is the persistent current energy of each qubit, Δ_k is the qubit energy gap when $\varepsilon_k = 0$, while $\hat{\sigma}_{zk}$ and $\hat{\sigma}_{xk}$ are the Pauli matrices for the k-th qubit. We define $\varepsilon_k > 0$ when the qubit current flows anticlockwise and vice versa.

After a unitary transformation that diagonalizes the atomic Hamiltonians $\hat{\mathcal{H}}_{qk}$, we obtain a generalized Dicke Hamiltonian[41] with

spin–spin interaction:

$$\hat{\mathcal{H}}_{tot}/\hbar \simeq \omega_r\hat{a}^\dagger\hat{a} + \frac{\omega_{q1}}{2}\hat{\sigma}_{z1} + \frac{\omega_{q2}}{2}\hat{\sigma}_{z2} - (g_1\hat{\Lambda}_1 - g_2\hat{\Lambda}_2)(\hat{a}^\dagger + \hat{a}) - \frac{2g_1g_2}{\omega_r}\hat{\Lambda}_1\hat{\Lambda}_2, \quad (6)$$

where $\omega_{qk} = \text{sgn}(\varepsilon_k)(\varepsilon_k^2 + \Delta_k^2)^{1/2}$ is the qubit frequency and $\hat{\Lambda}_k = (\cos\theta_k\,\hat{\sigma}_{xk} + \sin\theta_k\,\hat{\sigma}_{zk})$ gives the direction of the interaction, with $\theta_k \simeq -\arctan(\varepsilon_k/\Delta_k)$ (see Methods for more details). For $\theta_k = 0$ ($\varepsilon_k = 0$), the interaction is purely transverse. When $\theta_k \neq 0$, the interaction has a longitudinal component and the one-photon-exciting-two-atoms effect is allowed.

Energy spectrum

Figure 2a shows the raw data of the measured spectrum as a function of the persistent current energy ε_1 of qubit 1, which are obtained after fixing the value of $\varepsilon_2/2\pi$ at -3.22 GHz when $\varepsilon_1 = 0$. In Fig. 2b, the spectrum is fitted with the numerically calculated transition frequencies ω_{ij} between the i-th and j-th eigenstates of the total Hamiltonian $\hat{\mathcal{H}}_{tot}$. The persistent current energy for qubit 2 and the resonator frequency are affected by the external magnetic flux applied to qubit 1[8]. Thus, to derive the transition frequencies ω_{ij}, we substitute $\varepsilon_2 \rightarrow \varepsilon_2 + A\varepsilon_1$ and $\omega_r \rightarrow \omega_r(1 + B_\pm\varepsilon_1)$ in Eq. (5), where A and $B_\pm$ are small fitting parameters listed in Table 1. We use two different values for $B_\pm$ because the spectrum is asymmetric with respect to the sign of ε_1, i.e., B_+ is used when $\varepsilon_1 \geq 0$ and vice versa. Including A and $B_\pm$, we use 11 parameters in total for the fit. These also include the bias current offset I_{b0}, when $\varepsilon_1 = 0$, and the persistent current coefficient $\tilde{\varepsilon}_0$ to derive $\hbar\varepsilon_1 = I_p\Phi_0(\varphi_{e1} - 0.5) = \hbar\tilde{\varepsilon}_0(I_b - I_{b0})$, where I_p is the persistent current of qubit 1, and I_b is the bias current from the room-temperature current source. We use a photo-processing technique to obtain peak points from the spectrum[37,42,43] and the quantum toolbox in Python for numerical calculations[44,45].
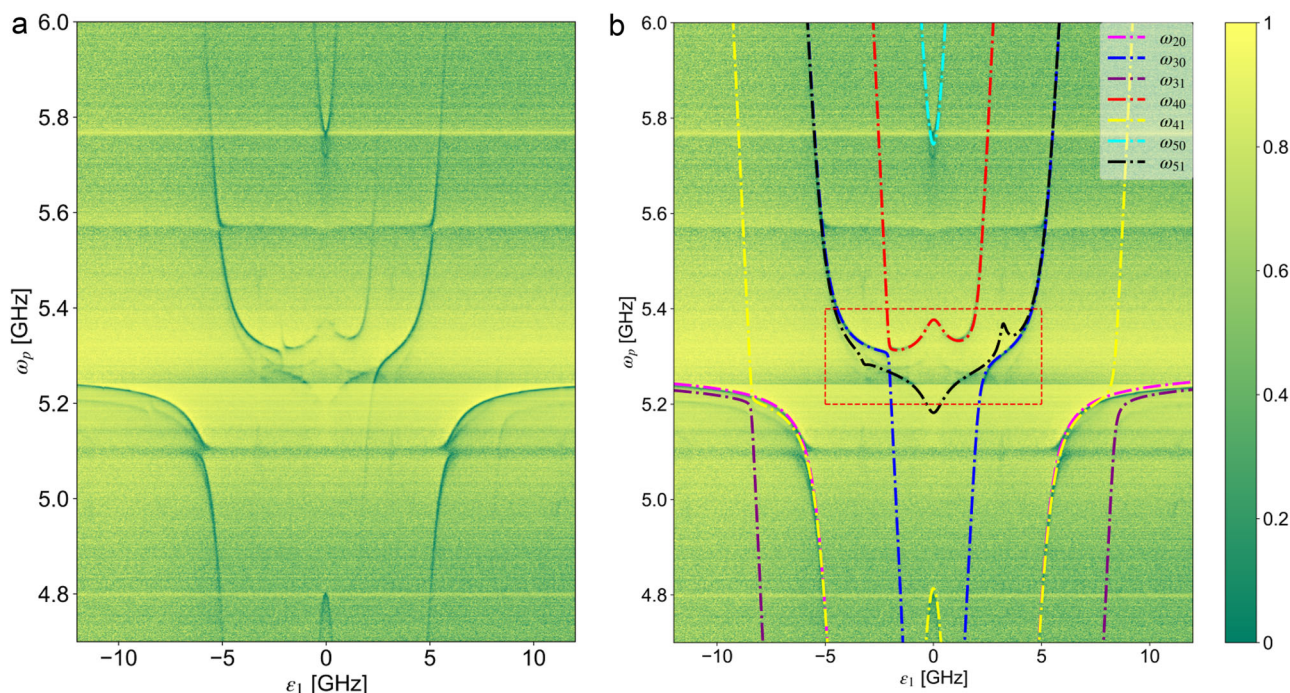

Fig. 2 | Transmission spectra. Pump frequency ω_p from the vector network analyzer versus the persistent current energy ε_1 of qubit 1. **a** Raw data of the observed single-tone spectrum of the sample shown in Fig. 1. **b** Observed single-tone spectrum with fitted curves corresponding to the state transition frequencies ω_{ij} between the i-th and j-th eigenstates of Hamiltonian (6). The fit parameters are $g_1/2\pi = 3.33$, $g_2/2\pi = 3.45$, $\Delta_1/2\pi = 1.31$, $\Delta_2/2\pi = 1.27$, $\omega_r/2\pi = 5.15$, and $\varepsilon_2/2\pi = -3.22$ GHz. At around $\omega_p/2\pi = 5.09$ GHz and 5.57 GHz, parasitic modes can be seen, which originate from, for example, sample ground planes and/or the measurement environment, which includes the sample holder and microwave components coupled to the system.

Flux qubits 1 and 2 are almost identical except for the loop size; consequently, they have similar fitting parameters; i.e., $\Delta_{q1} \simeq \Delta_{q2} \simeq 0.25\,\omega_r$. We find atom-resonator coupling rates of $g_1/\omega_r = 0.67$ and $g_2/\omega_r = 0.69$, indicating that the artificial atoms are ultrastrongly coupled with the resonator.

One photon simultaneously excites two atoms

We indicate with $|\psi_i\rangle$ the eigenstate of the system Hamiltonian $\hat{\mathcal{H}}_{tot}$ with eigenenergies $\hbar\omega_{i0}$. The $\omega_{qi}\hat{\sigma}_{zi}/2$ terms in Eq. (6) define the ground $|g\rangle$ and excited $|e\rangle$ atomic bare states.

In Fig. 3a, which is an enlarged view of the red dashed rectangle in Fig. 2b, the black arrow indicates the anticrossing between the

Table 1 | List of the fitting parameters used in Figs. 2 and 3

Name	Symbol	Value	Unit
Resonator frequency	$\omega_r/2\pi$	5.15	GHz
Coupling constant of Q_1	$g_1/2\pi$	3.33	GHz
Coupling constant of Q_2	$g_2/2\pi$	3.45	GHz
Energy gap of Q_1	$\Delta_1/2\pi$	1.31	GHz
Energy gap of Q_2	$\Delta_2/2\pi$	1.27	GHz
Persistent current energy of Q_2	$\varepsilon_2/2\pi$	−3.22	GHz
Persist current coefficient	$\tilde{\varepsilon}_0/2\pi$	201.6	GHz/mA
Bias current offset	I_{b0}	0.547	mA
Crosstalk coefficient	A	−9.43	×10^{-3}
Res. freq. modification $\varepsilon_1 > 0$	B_+	0.78	×10^{-3}
Res. freq. modification $\varepsilon_1 < 0$	B_-	0.73	×10^{-3}

We use the first eight listed parameters for an initial fit. Afterwards, we add the last three parameters to slightly modify the fit. The initial parameters ω_r, $\tilde{\varepsilon}_0$, and I_{b0} can be obtained from the spectrum. Also, the qubit parameters g_i and Δ_i can be estimated from the design parameters.

eigenstates $|\psi_3\rangle$ and $|\psi_4\rangle$ (see Fig. 3b), with eigenfrequencies ω_{30} and ω_{40}. In agreement with this anticrossing, Fig. 3c shows the numerically calculated projection $P_j^{(i)} \equiv |\langle\psi_i|j\rangle|^2$ of the third and fourth eigenstates $|\psi_i\rangle$ $(i = 3, 4)$ on the bare states $|j\rangle = \{|gg1\rangle, |ee0\rangle\}$ as a function of ε_1. Here, it is possible to see that the third and fourth eigenstates are the approximate symmetric and antisymmetric superpositions of $|gg1\rangle$ and $|ee0\rangle$, respectively. Considering also that the sum of the dressed qubit frequencies is nearly equal to the dressed resonator frequency, the anticrossing is the signature of the one–photon–exciting–two–atoms effect (see Methods for more details). Half of the minimum split between ω_{30} and ω_{40} in the spectrum gives the effective coupling between $|gg1\rangle$ and $|ee0\rangle$, that is 22.8 MHz (see Supplementary Information).

With respect to the theoretical prediction in ref. 28 ($g/\omega_r \simeq 0.1$–0.2), our system has a much larger coupling ($g/\omega_r \simeq 0.7$). This implies that the system eigenstates should have a strong dressing, and in principle we could not observe a clean "one–photon–exciting–two–atoms" effect. On the contrary, Fig. 3c shows that the dressing is low for those states, and, as shown in Fig. 5, our system can still be considered formed by two separated two-level atoms and one cavity mode with shifted eigenfrequencies. This behavior is heuristically justified by the fact that spin–spin and spins–light couplings are competing interactions and that the longitudinal interaction "decouples" for specific values of the signs of ε_1 and ε_2. The signature of this "longitudinal decoupling" is given by the asymmetry in the spectrum with respect to the sign of ε_1. Assuming that there are only longitudinal couplings, in the interaction part of Eq. (6), the operator $(\hat{a}^\dagger + \hat{a})$ should generate coherent states of light in the ultrastrong coupling regime[46]. However, considering $\varepsilon_1 < 0$ and $\varepsilon_2 < 0$, the atomic states are not associated with coherent states if $M = m_1 - m_2 = 0$, where $m_k = \pm1$ is the eigenstate of $\hat{\sigma}_{zk}$ ($k = 1, 2$) (see Methods for more details). As a result, the ground $|gg\rangle$ and excited $|ee\rangle$ states, which have $M = 0$, have no coherent states associated with them. Nevertheless, the transverse interactions still affect our system, generating a small dressing that reduces the projections $P_{gg1}^{(4)}$ and $P_{ee0}^{(3)}$ to almost 0.8 at $\varepsilon_1/2\pi = -2.4$ GHz.
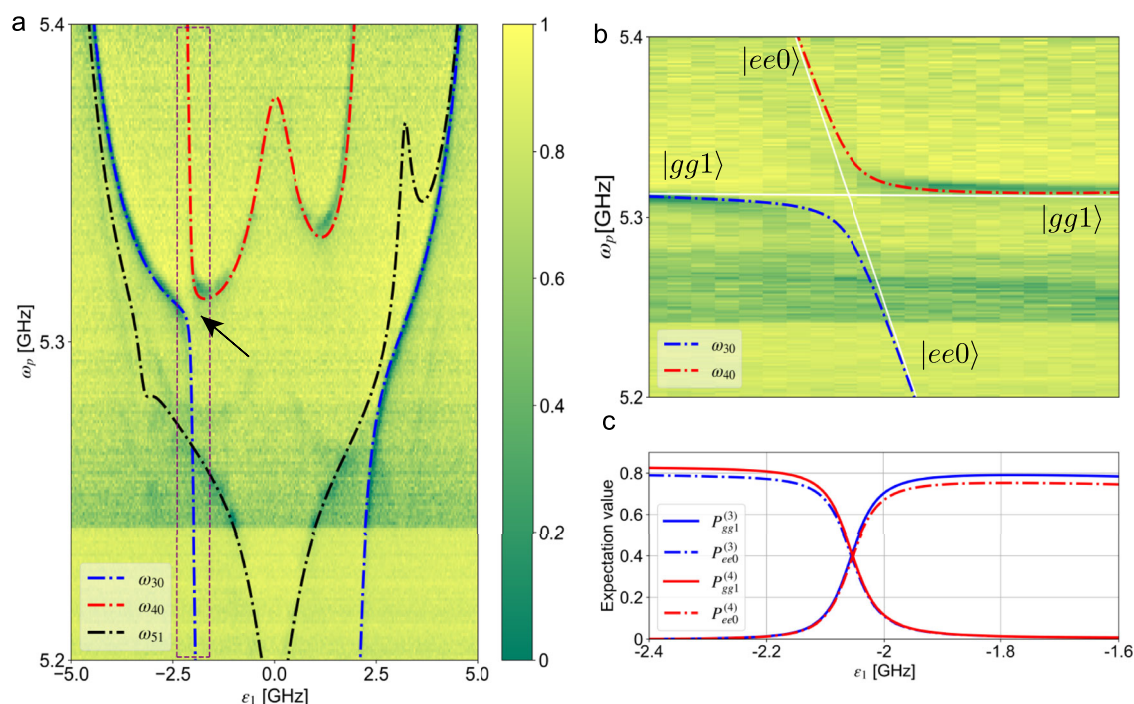

Fig. 3 | Anticross between $|gg1\rangle$ and $|ee0\rangle$. a Enlarged view of the central part of the spectrum in Fig. 2b with fitting curve. The fitting reproduces the spectrum well. **b** Enlarged image of the anticrossing between ω_{30} and ω_{40}. The white lines represent the eigenmodes of $|gg1\rangle$ and $|ee0\rangle$ in the non-interacting Hamiltonian (see Methods for more details). **c** Projection of the third and fourth eigenstates calculated using Hamiltonian in Eq. (6) with the fitting parameters to the bare states $|gg1\rangle$ and $|ee0\rangle$.

Discussion

We measured the spectrum of a circuit composed of two artificial atoms ultrastrongly coupled to an *LC* resonator. The generalized Dicke Hamiltonian with spin–spin interaction correctly describes the measured spectrum. At the energy where the sum of the atomic energies almost matches that of the resonator, we observed one anticrossing between the states $|gg1\rangle$ and $|ee0\rangle$. This experimentally confirms the recent theoretical prediction that one photon can simultaneously excite two atoms[28], opening a new chapter in quantum nonlinear optics.

Clearly, only the avoided-level crossing and not the excitation process itself have been experimentally observed, because our experiment was not designed to observe Rabi oscillations. However, our spectroscopic observations prove the existence of this excitation. Future work will involve reading out the qubit and photon states[47] as well as observing the one-photon–exciting–two-atoms dynamics. Theoretically, the reduction of dressing and the asymmetry in the spectrum could be further investigated. These studies could also be extended to explore, for example, photon down- and up-conversions[27,48] and ultrafast two-qubit gates[14,17].

Methods

Circuit Hamiltonian

Here, we describe the circuit Hamiltonian calculation in detail. The branch fluxes across the circuit elements, which are Josephson junctions, the inductance L_r, and the capacitance C_r, follow Kirchhoff's voltage laws:

$$\varphi_{\beta 1} + \varphi_{\alpha 1} + \varphi_{a1} + \varphi_{b1} = \varphi_{e1}, \tag{7}$$

$$\varphi_{\beta 2} + \varphi_{\alpha 2} + \varphi_{a2} + \varphi_{b2} = \varphi_{e2}, \tag{8}$$

$$\varphi_{cr} + \varphi_r + \varphi_{\beta 1} - \varphi_{\beta 2} = 0, \tag{9}$$

where φ_{cr} and $\varphi_{\ell r}$ represent fluxes between the resonator capacitor and the inductor. The total Lagrangian of the circuit is

$$\mathcal{L}_{tot} = \mathcal{K}_{J1} + \mathcal{K}_{J2} - \mathcal{U}_{J1} - \mathcal{U}_{J2} + \mathcal{L}_r, \tag{10}$$

where

$$\mathcal{K}_{Jk} = \frac{C_J}{2}\left[\beta \dot{\phi}_{\beta k}^2 + \dot{\phi}_{ak}^2 + \dot{\phi}_{bk}^2 + \alpha_i(\dot{\phi}_{\beta k} + \dot{\phi}_{ak} + \dot{\phi}_{bk})^2 \right], \tag{11}$$

$$\mathcal{U}_{Jk} = -E_J\left[\beta_i \cos(\varphi_{\beta k}) + \cos(\varphi_{ak}) + \cos(\varphi_{bk}) + \alpha_i \cos(\varphi_{ek} - \varphi_{\beta k} - \varphi_{ak} - \varphi_{bk}) \right], \tag{12}$$

$$\mathcal{L}_r = \frac{C_r}{2}\dot{\phi}_{cr}^2 - \frac{1}{2L_r}(\phi_{cr} + \phi_{\beta 1} - \phi_{\beta 2})^2. \tag{13}$$

Here, $k \in \{1, 2\}$ indicates the qubit, and the sub-index cr indicates the capacitor of the resonator. The qubit kinetic energy part of the Lagrangian in Eq. (10) becomes

$$\mathcal{K}_{Ji} = \frac{1}{2}\dot{\phi}^T M \dot{\phi}, \tag{14}$$

where $\boldsymbol{\phi}_k \equiv \left(\phi_{\beta k} \phi_{ak} \phi_{bk} \right)^T$ and the mass matrix is given by

$$M_k = C_J \begin{pmatrix} \beta_k + \alpha_k & \alpha_k & \alpha_k \\ \alpha_k & 1 + \alpha_k & \alpha_k \\ \alpha_k & \alpha_k & 1 + \alpha_k \end{pmatrix}. \tag{15}$$

Using the canonical conjugate $q_i = \partial L_{tot}/\partial \dot{\phi}_i$ for $\dot{\phi}_i$, where $i \in \{\beta_k, a_k, b_k\}$, we can rewrite Eq. (14) as

$$\mathcal{K}_{Jk} = \frac{1}{2}\mathbf{q}_k^T M^{-1} \mathbf{q}_k. \tag{16}$$

Then, we obtain the total Hamiltonian of the circuit as

$$\begin{aligned}\mathcal{H}_{tot} &= \sum_k \mathbf{q}_k^T \dot{\boldsymbol{\phi}}_k - \mathcal{L}_{tot} \\ &= \sum_k (4E_c \tilde{\mathbf{q}}_k^T \tilde{M}_k^{-1} \tilde{\mathbf{q}}_k + E_{Lr}\varphi_{\beta k}^2 + \mathcal{U}_{Jk}) \\ &\quad + \mathcal{H}_r + \mathcal{H}_{int}, \end{aligned} \tag{17}$$

where $2e\tilde{q} = q$ and $C_J \tilde{M} = M$. The term $E_{Lr}\varphi_{\beta k}$ originates from Eq. (13) since we define

$$\mathcal{H}_r \equiv \frac{C_r}{2}\dot{\phi}_{cr}^2 + \frac{1}{2L_r}\phi_{cr}^2 \tag{18}$$

as a bare *LC* resonator. We now replace the canonical values with the operators $\varphi \to \hat{\varphi}$ and $q \to \hat{q}$ and impose their relation $[\hat{\varphi}, \hat{q}] = i$. For the resonator, we introduce the creation and annihilation operators. Thereafter, we expand the quantized total Hamiltonian using the eigenvectors $|i\rangle_i$ ($i \in \mathbb{N}$) of the atom Hamiltonians ($\hat{\mathcal{H}}_{tot} - \hat{\mathcal{H}}_r - \hat{\mathcal{H}}_{int}$),

$$\begin{aligned}\hat{\mathcal{H}}_{tot} &= \hbar \sum_i (\Omega_i^{(1)}|i\rangle_1\langle i|_1 + \Omega_i^{(2)}|i\rangle_2\langle i|_2) + \hat{\mathcal{H}}_r \\ &\quad - \hbar \sum_{i,j} (g_{ij}^{(1)}|i\rangle_1\langle j|_1 - g_{ij}^{(2)}|i\rangle_2\langle j|_2)(\hat{a}^\dagger + \hat{a}) \\ &\quad - E_L \sum_{i,j} g_{ij}^{(1)} g_{ij}^{(2)}|i\rangle_1|i\rangle_2\langle j|_1\langle j|_2, \end{aligned} \tag{19}$$

where $\hbar\Omega_i^{(k)}$ is the *i*-th eigenenergy of atom *k* and $\hbar g_{ij}^{(k)} = I_{zpf}\Phi_0 \langle i|\hat{\varphi}_{\beta k}|j\rangle$ is the coupling matrix element ($I_{zpf} = \sqrt{\hbar\omega_r/2L_r}$). After truncating the higher state of the flux qubits, we obtain the Hamiltonian of two two-level atoms and a resonator, Eqs. (5) and (6). In Eqs. (5) and (6), the
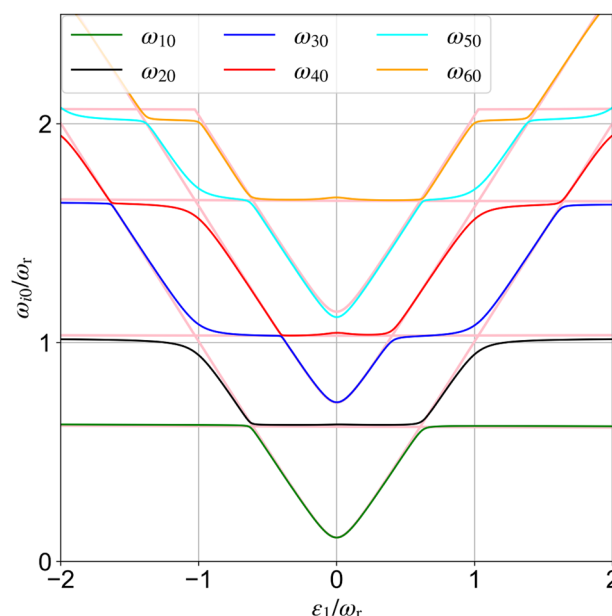

Fig. 4 | Comparison between the lowest eigenstates of the Hamiltonian in Eq. (6) and the non-interacting Hamiltonian (light pink curves). The non-interacting Hamiltonian is derived from Eq. (6) with $g_1 = g_2 = 0$, shifting the atom frequencies. The shifts are chosen such that $\Delta_{1,2} \to \Delta_{1,2} \exp -2(g_{1,2}/\omega_r)^2$. For simplicity, we ignore the qubit bias current crosstalk, A = 0.
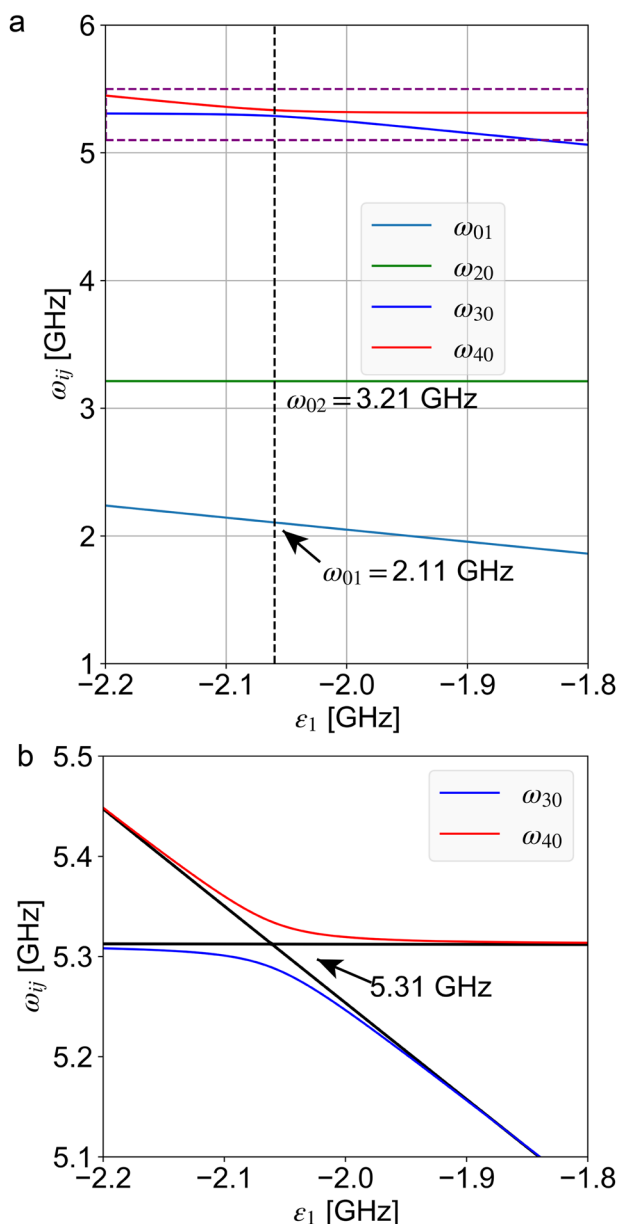
Fig. 5 | Energy levels at the bias point of the anticross. a Numerically calculated spectrum as a function of ε_1 around the anticross point between ω_{30} and $\omega_{40}(\varepsilon_1 < 0)$. **b** Enlarged image of the purple dashed square in **a**. Black lines show ω_{30} and ω_{40} derived from the non-interacting Hamiltonian.

spin–spin interaction reduces the current flowing in the resonator loop, which in this system is the ferromagnetic coupling.

One–photon two–atoms energy exchange

Figure 4 shows numerically calculated transition frequencies of the system using the fit parameters over a wider range. For comparison, we overlaid the eigenvalues of the Hamiltonian in Eq. (6) with the eigenvalues calculated when $g_1 = g_2 = 0$. In the latter case, we shifted the atoms and cavity frequencies to consider the dressing effect. From Fig. 4, it is possible to notice that the eigenvalues of the interacting and non-interacting ($g_1 = g_2 = 0$) Hamiltonians almost coincide, proving that our system, operating in the ultrastrong coupling regime, can still be considered composed of two independent atoms and a resonator that interact in the crossing points. Figure 5a is an enlarged image of Fig. 4, with the range around the anticrossing between ω_{30} and $\omega_{40}(\varepsilon_1 < 0)$. In our circuit, ω_{01} and ω_{02} are the frequencies of dressed qubits 1 and 2, respectively. From the enlarged image of the

Table 2 | Possible values of M and relative states. We consider ε₂ < 0

m_1	−1	+1	−1	+1
m_2	−1	−1	+1	+1
M_-	0	+2	−2	0
States if $\varepsilon_1 < 0$	$|gg\rangle|0\rangle$	$|eg\rangle|-\alpha\rangle$	$|ge\rangle|+\alpha\rangle$	$|ee\rangle|0\rangle$
M_+	+2	0	0	−2
States if $\varepsilon_1 > 0$	$|gg\rangle|+\alpha\rangle$	$|eg\rangle|0\rangle$	$|ge\rangle|0\rangle$	$|ee\rangle|-\alpha\rangle$

anticrossing in Fig. 5a, b, it is possible to see that the transition frequency of $|gg1\rangle$ at the anticrossing point is 5.312 GHz, which is close to the sum of the frequencies of the dressed qubits, $\omega_{01} + \omega_{02} = 5.318$ GHz.

It has been shown that when an atom interacts longitudinally with light, the atomic states are associated with coherent states of light[46]. In our system, the generation of coherent states, given by the longitudinal coupling of the atoms with the resonator, depends on the signs of ε_1 and ε_2. In the following derivation, we show that when $\varepsilon_1 < 0$ and $\varepsilon_2 < 0$, the atomic states $|ge\rangle$ and $|eg\rangle$ are associated with the coherent states of light, while states $|gg\rangle$ and $|ee\rangle$ are not associated with those.

Considering the system Hamiltonian [Eq. (6)] with $\Delta_k = 0$, $g_1 = g_2 = g$, and substituting σ_{zk} with its eigenvalue $m_k = \pm 1$, we can write the following:

$$\hat{\mathcal{H}}_s/\hbar = \frac{|\varepsilon_1|}{2}m_1 + \frac{|\varepsilon_2|}{2}m_2 + \omega_r \hat{a}^\dagger \hat{a} + gM(\hat{a}^\dagger + \hat{a}), \tag{20}$$

with $M = \text{sgn}(\varepsilon_2)m_2 - \text{sgn}(\varepsilon_1)m_1$. Performing the substitution $\hat{a} = \hat{b} - Mg/\omega_r$, we obtain

$$\hat{\mathcal{H}}_s/\hbar = \omega_r \hat{b}^\dagger \hat{b} + \frac{|\varepsilon_1|}{2}m_1 + \frac{|\varepsilon_2|}{2}m_2 - M^2\frac{g^2}{\omega_r}, \tag{21}$$

which is the Hamiltonian of a harmonic oscillator. By applying the annihilation operator $\hat{b}$ to its ground state $|0\rangle_M$ (i.e., $\hat{b}|0\rangle_M = 0$), we have

$$\hat{a}|0\rangle_M = -M\frac{g}{\omega_r}|0\rangle_M. \tag{22}$$

From Eq. (22), we see that atomic states with $M = 0$ are associated with the zero-photon state; while atomic states with $M = \pm 2$ are associated with photonic coherent states $|\pm\alpha\rangle$. In turn, M depends on the signs of ε_1 and ε_2. If $\varepsilon_1 < 0$ and $\varepsilon_2 < 0$, then $M_- \equiv M = m_1 - m_2$. If $\varepsilon_1 > 0$ and $\varepsilon_2 < 0$, then $M_+ \equiv M = -(m_1 + m_2)$. Table 2 shows the eight possible states as a function of the sign of ε_1 when the interaction is longitudinal. This explains the asymmetry of the spectra with respect to the sign of ε_1.

Data availability

All figures and results in this study can be reproduced using the CSV data and code provided in the supplementary information. All data are available in the main text or supplementary information, including the relevant CSV and TXT files.

Code availability

All custom codes used in this study are provided as text files in the Supplementary Information.

References

1. Nakamura, Y., Pashkin, Y. A. & Tsai, J. S. Coherent control of macroscopic quantum states in a single-cooper-pair box. *Nature* **398**, 786 (1999).

2. Gu, X., Kockum, A. F., Miranowicz, A., Liu, Y.-x. & Nori, F. Microwave photonics with superconducting quantum circuits. *Phys. Rep.* **718-719**, 1 (2017).

3. Krantz, P. et al. A quantum engineer's guide to superconducting qubits. *Appl. Phys. Rev.* **6**, 021318 (2019).

4. Kjaergaard, M. et al. Superconducting qubits: current state of play. *Annu. Rev. Condens. Matter Phys.* **11**, 369 (2020).

5. Blais, A., Grimsmo, A. L., Girvin, S. M. & Wallraff, A. Circuit quantum electrodynamics. *Rev. Mod. Phys.* **93**, 025005 (2021).

6. Kwon, S., Tomonaga, A., Lakshmi Bhai, G., Devitt, S. J. & Tsai, J.-S. Gate-based superconducting quantum computing. *J. Appl. Phys.* **129**, 041102 (2021).

7. Niemczyk, T. et al. Circuit quantum electrodynamics in the ultrastrong-coupling regime. *Nat. Phys.* **6**, 772 (2010).

8. Yoshihara, F. et al. Superconducting qubit-oscillator circuit beyond the ultrastrong-coupling regime. *Nat. Phys.* **13**, 44 (2017).

9. Forn-Díaz, P. et al. Ultrastrong coupling of a single artificial atom to an electromagnetic continuum in the nonperturbative regime. *Nat. Phys.* **13**, 39 (2017).

10. Bosman, S. J. et al. Multi-mode ultra-strong coupling in circuit quantum electrodynamics. *npj Quant. Inf.* **3**, 1 (2017).

11. Ao, Z. et al. Extremely large Lamb shift in a deep-strongly coupled circuit QED system with a multimode resonator. *Sci. Rep.* **13**, 11340 (2023).

12. Frisk Kockum, A., Miranowicz, A., De Liberato, S., Savasta, S. & Nori, F. Ultrastrong coupling between light and matter. *Nat. Rev. Phys.* **1**, 19 (2019).

13. Forn-Díaz, P., Lamata, L., Rico, E., Kono, J. & Solano, E. Ultrastrong coupling regimes of light-matter interaction. *Rev. Mod. Phys.* **91**, 025005 (2019).

14. Romero, G., Ballester, D., Wang, Y. M., Scarani, V. & Solano, E. Ultrafast Quantum Gates in Circuit QED. *Phys. Rev. Lett.* **108**, 120501 (2012).

15. Kyaw, T. H., Herrera-Martí, D. A., Solano, E., Romero, G. & Kwek, L.-C. Creation of quantum error correcting codes in the ultrastrong coupling regime. *Phys. Rev. B* **91**, 064503 (2015).

16. Wang, Y., Zhang, J., Wu, C., You, J. Q. & Romero, G. Holonomic quantum computation in the ultrastrong-coupling regime of circuit QED. *Phys. Rev. A* **94**, 012328 (2016).

17. Wang, Y., Guo, C., Zhang, G.-Q., Wang, G. & Wu, C. Ultrafast quantum computation in ultrastrongly coupled circuit QED systems. *Sci. Rep.* **7**, 44251 (2017).

18. Stassi, R., Cirio, M. & Nori, F. Scalable quantum computer with superconducting circuits in the ultrastrong coupling regime. *npj Quant. Inf.* **6**, 1 (2020).

19. Chen, Y.-H., Qin, W., Stassi, R., Wang, X. & Nori, F. Fast binomial-code holonomic quantum computation with ultrastrong light-matter coupling. *Phys. Rev. Res.* **3**, 033275 (2021).

20. Liberato, S. D., Ciuti, C. & Carusotto, I. Quantum vacuum radiation spectra from a semiconductor microcavity with a time-modulated vacuum Rabi frequency. *Phys. Rev. Lett.* **98**, 103602 (2007).

21. Ashhab, S. & Nori, F. Qubit-oscillator systems in the ultrastrong-coupling regime and their potential for preparing nonclassical states. *Phys. Rev. A* **81**, 042311 (2010).

22. Stassi, R., Ridolfo, A., Di Stefano, O., Hartmann, M. J. & Savasta, S. Spontaneous conversion from virtual to real photons in the ultrastrong-coupling regime. *Phys. Rev. Lett.* **110**, 243601 (2013).

23. Cirio, M., De Liberato, S., Lambert, N. & Nori, F. Ground state electroluminescence. *Phys. Rev. Lett.* **116**, 113601 (2016).

24. Stassi, R. et al. Unveiling and veiling an entangled light-matter quantum state from the vacuum. *Phys. Rev. Res.* **5**, 043095 (2023).

25. Garziano, L. et al. Multiphoton quantum Rabi oscillations in ultrastrong cavity QED. *Phys. Rev. A* **92**, 063830 (2015).

26. Stassi, R. et al. Quantum nonlinear optics without photons. *Phys. Rev. A* **96**, 023818 (2017).

27. Kockum, A. F., Miranowicz, A., Macrì, V., Savasta, S. & Nori, F. Deterministic quantum nonlinear optics with single atoms and virtual photons. *Phys. Rev. A* **95**, 063849 (2017).

28. Garziano, L. et al. One Photon Can Simultaneously Excite Two or More Atoms. *Phys. Rev. Lett.* **117**, 043601 (2016).

29. Ball, P. Two atoms can jointly absorb one photon. *Physics* **9**, 83 (2016).

30. Garziano, L., Stassi, R., Ridolfo, A., Di Stefano, O. & Savasta, S. Vacuum-induced symmetry breaking in a superconducting quantum circuit. *Phys. Rev. A* **90**, 043817 (2014).

31. Wang, S.-P. et al. Probing the symmetry breaking of a light-matter system by an ancillary qubit. *Nat. Commun.* **14**, 4397 (2023).

32. Mehta, N., Kuzmin, R., Ciuti, C. & Manucharyan, V. E. Down-conversion of a single photon as a probe of many-body localization. *Nature* **613**, 650 (2023).

33. Miyanaga, T., Tomonaga, A., Ito, H., Mukai, H. & Tsai, J. Ultrastrong tunable coupler between superconducting *LC* resonators. *Phys. Rev. Appl.* **16**, 064041 (2021).

34. Zotova, J. et al. Compact superconducting microwave resonators based on Al-AlO x-Al capacitors. *Phys. Rev. Appl.* **19**, 044067 (2023).

35. Kroll, J. et al. Magnetic-field-resilient superconducting coplanar-waveguide resonators for hybrid circuit quantum electrodynamics experiments. *Phys. Rev. Appl.* **11**, 064053 (2019).

36. Chiorescu, I. et al. Coherent dynamics of a flux qubit coupled to a harmonic oscillator. *Nature* **431**, 159 (2004).

37. Tomonaga, A., Mukai, H., Yoshihara, F. & Tsai, J. S. Quasiparticle tunneling and $1/f$ charge noise in ultrastrongly coupled superconducting qubit and resonator. *Phys. Rev. B* **104**, 224509 (2021).

38. Billangeon, P.-M., Tsai, J. S. & Nakamura, Y. Circuit-QED-based scalable architectures for quantum information processing with superconducting qubits. *Phys. Rev. B* **91**, 094517 (2015).

39. Robertson, T. L. et al. Quantum theory of three-junction flux qubit with non-negligible loop inductance: towards scalability. *Phys. Rev. B* **73**, 174526 (2006).

40. Yoshihara, F., Ashhab, S., Fuse, T., Bamba, M. & Semba, K. Hamiltonian of a flux qubit-LC oscillator circuit in the deep-strong-coupling regime. *Sci. Rep.* **12**, 6764 (2022).

41. Jaako, T., Xiang, Z.-L., Garcia-Ripoll, J. J. & Rabl, P. Ultrastrong-coupling phenomena beyond the Dicke model. *Phys. Rev. A* **94**, 033850 (2016).

42. Sato, Y. et al. Three-dimensional multi-scale line filter for segmentation and visualization of curvilinear structures in medical images. *Med. Image Anal.* **2**, 143 (1998).

43. Walt, Svd et al. scikit-image: image processing in Python. *PeerJ* **2**, e453 (2014).

44. Johansson, J. R., Nation, P. D. & Nori, F. QuTiP: an open-source Python framework for the dynamics of open quantum systems. *Computer Phys. Commun.* **183**, 1760 (2012).

45. Johansson, J. R., Nation, P. D. & Nori, F. QuTiP 2: a Python framework for the dynamics of open quantum systems. *Comput. Phys. Commun.* **184**, 1234 (2013).

46. Stassi, R. & Nori, F. Long-lasting quantum memories: extending the coherence time of superconducting artificial atoms in the ultrastrong-coupling regime. *Phys. Rev. A* **97**, 033823 (2018).

47. Felicetti, S., Douce, T., Romero, G., Milman, P. & Solano, E. Parity-dependent state engineering and tomography in the ultrastrong coupling regime. *Sci. Rep.* **5**, 11818 (2015).

48. Inomata, K. et al. Microwave down-conversion with an impedance-matched Λ system in driven circuit QED. *Phys. Rev. Lett.* **113**, 063604 (2014).

Acknowledgements

Author contributions

A.T. designed the device, carried out the experiment, and analyzed the data. R.S. and A.T. performed theoretical and numerical calculations. H.M. carried out part of the experiment. F.N., F.Y., and J.S.T. participated in discussions and contributed to the writing and editing of the manuscript. J.S.T. also conducted the research and managed the laboratory. All authors contributed to the manuscript preparation and revision.

Competing interests

The authors declare no competing interests.

Additional information

Supplementary information The online version contains supplementary material available at
https://doi.org/10.1038/s41467-025-60589-5.

Correspondence and requests for materials should be addressed to A. Tomonaga or J. S. Tsai.

Peer review information *Nature Communications* thanks Fernando Lombardo and the other, anonymous, reviewer(s) for their contribution to the peer review of this work. A peer review file is available.

Reprints and permissions information is available at
http://www.nature.com/reprints

Publisher's note Springer Nature remains neutral with regard to jurisdictional claims in published maps and institutional affiliations.